Closed loop control of vibration field transient: Application to wave focusing

Anis Kaci, Christophe Giraud-Audine, Frédéric Giraud, Michel Amberg, Betty Lemaire-Semail

Closed loop control of vibration field transient: application to wave focusing

Anis Kaci, Christophe Giraud-Audine*, Frederic Giraud, Michel Amberg,
Betty Lemaire-Semail

*Univ. Lille, Arts et Métiers Institute of Technology, Centrale Lille, Junia, ULR 2697 -
L2EP, F-59000 Lille, France*

Abstract

In this article, several modes are controlled simultaneously both in phase and amplitude on an haptic display. To achieve this, modulation/demodulation control combined with mixed spatial/frequency filters is developed. It is then applied to produce a predefined velocity field both in space and time on a plate. The experimental results show good agreement with theory.

Keywords: modulated-demodulated control (Vector control), Multimodal vibration control, modal decomposition , focusing, Modal filter, Piezoelectric transducer, Linear Quadratic Regulator (LQR)

1. Introduction

In some applications, the excitation of the modes of a structure is unwanted as it leads to detrimental effects, like failures [1]. For that purpose, passive or active control methods have been deployed in order to damp those vibrations. In other applications however, a perfect harmonic vibration of the structure, at a given amplitude is necessary. This is the case for Atomic force microscopy (AFM) [2], Micro Electro-Mechanical Systems (MEMS) [3], and the burgeoning field of haptic interfaces [4]. The main issues for these typical applications are the robustness of the amplitude besides external perturbation as well as the fact that these devices operate at several kHz.

---

*Corresponding author
Email address: christophe.giraud-audine@ensam.eu (Christophe Giraud-Audine)

Researchers have proposed closed loop controls in order to deal with these issues. Autoresonance is a non-linear feedback control technique that allows to automatically excite a vibration mode at its natural frequency while imposing the vibration amplitude [5]. The modulated-demodulated control [6] is an adaptive control approach which was introduced in the 90's in order to reject sinusoidal perturbations [7, 8]. This technique consists in demodulating the measured vibration by a sinusoidal signals, named the carrier, in order to obtain the real (direct) and imaginary (quadrature) components of the vibration. A controller is then implemented on these components to deduce therefrom the demodulated control effort, which is modulated by the carrier. In [9], the authors introduce the Vector Control method which encompasses the dynamic amplitude control during transients, with the tracking of the system's resonance frequency. Improved dynamic performances as well as efficient operation are obtained, yet at simplified practical implementation [10].

For some recent applications it is interesting to use several modes which dynamics and synchronization are ensured. For instance, in a bi-modal Atomic Force Microscopy, a first bending mode is used for topography imaging and a second one gives mechanical and electromagnetic properties of a studied sample [11]. In other applications, more than one vibration mode are excited, as to produce travelling waves for ultrasonic motor [12], it is also used for haptic interface to produce localized stimulation by modal superposition [13]. In energy harvester, the multimodal approach [14, 15] increases the efficiency of the system to extract more power, compared to a single degree of freedom harvester.

This work demonstrate the possibility to combine several techniques to achieve the control of several modes simultaneously, both in amplitude and phase. The application intended here is an haptic display, where localized stimulation will be rendered. This is obtain through rapid focusing, and by realizing specific velocity fields. This raises several challenges due to constraints such as the reduced number of sensors, decoupling parallel banks of controllers, and limited number of actuators.

The paper is organized as follows. The section 2 recalls the modal dynamic model of one vibration mode in its demodulated base the design of a controller described in [16] and addresses the control of several modes. In section 3, the experimental device is presented and different design protocols are developed specifically. Finally, in section 4, the different approaches developed in this article are validated through several experiments with good results.

2. Method

2.1. Modal dynamic model

In this section, we consider the general scheme of the studied system as shown in the Fig. 1. It consists in a vibrating structure with a displacement field $\boldsymbol{w}(\boldsymbol{x}, t)$ where $\boldsymbol{x}$ is the space coordinate. The structure is actuated through n_a actuators located in different point of the surface and the vibration of the structure is measured by using a set of n_s dispersed sensors
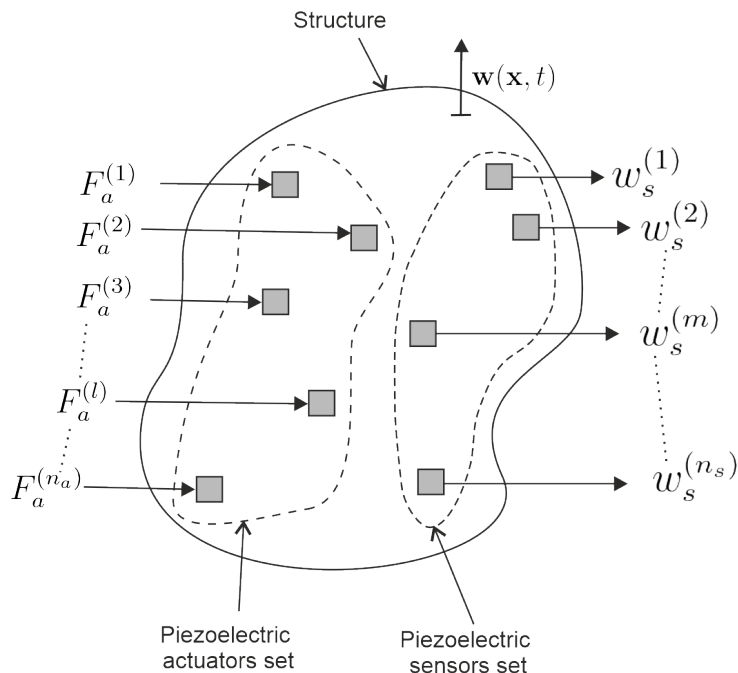

Figure 1: General scheme of the studied system , where the vibrating structure is controlled through a set of piezoelectric actuators and a set of piezoelectric sensors.

If the dynamic equations are described by self-adjoints operators, one can write using the modal decomposition [17] this displacement field as an infinite weighted sum of its mode shapes $\boldsymbol{\psi}^{(k)}(\boldsymbol{x})$:

$$\boldsymbol{w}(\boldsymbol{x}, t) = \sum_{k=1}^{\infty} \boldsymbol{\psi}^{(k)}(\boldsymbol{x}) \eta^{(k)}(t) \tag{1}$$

where the k$^{\text{th}}$ modal coordinates $\eta^{(k)}(t)$ verifies the dynamic equation:

$$\ddot{\eta}^{(k)}(t) + 2\xi_k \omega_k \dot{\eta}^{(k)}(t) + \omega_k^2 \eta^{(k)}(t) = f^{(k)}(t) \tag{2}$$

3

which is obtained by projection of the actual dynamic equation on the mode shapes normalized with respect to the mass. This procedure eliminates the spatial dependence of the problem, and provides a set of independent ordinary differential equations. In (2), ξ_k are the damping and ω_k the resonant frequency of the kth mode respectively, while $f^{(k)}$ is the modal effort resulting from the projection process.

In order to introduce some of the design constraints addressed in the following section, assume that the n_a actuators of the Fig. 1 produce the forces F_a at their respective location x_a ($a \in \{1, \ldots, n_a\}$). The modal projection process gives the following modal forces :

$$f^{(k)}(t) = \sum_{i=1}^{n_a} f_a^{(i)}(t) = \sum_{i=1}^{n_a} \boldsymbol{\psi}^{(k)}(x_a) F_a(t) \tag{3}$$

This leads to the observation that to efficiently transfer energy to a mode k, the actuators should be adequately located. Moreover, the Laplace transform of the modal velocities (which are of interest in this paper) is

$$\mathcal{L}[\dot{\eta}](s) = s\mathcal{L}[\eta] = \sum_{i=1}^{n_a} \psi^{(k)}(x_a)\mathcal{L}[F_a](t)\frac{s}{s^2 + 2\xi_i\omega_i s + \omega_i^2} \tag{4}$$

Hence each mode acts as an band pass filter with respect to the modal force. Therefore, to reduce the control effort, it must be ensured that the forces $F_a(t)$ have frequencies within the bandwidth of a given mode.. This later requirement motivates the use of the control proposed in the next section.

2.2. Dynamic modal model in a demodulated base

The aim of the application is to impose a specified velocity field and to control its transient. To this end, it is required to control simultaneously the relative amplitudes and phases of several modes. Since each mode should be excited close to or at its resonant frequency, it make sense to apply a modulated/demodulated control approach. In Fig. 2 the principle is illustrated in the case of the control a single degrees of freedom oscillator equivalent to Eq. 2. The vibration measurement $\eta(t)$ is demodulated by multiplying it by two sinusoidal signals in quadrature, then passing the resulting signals through low-pass filters. The benefit of the processing is to extract the envelop of $\eta(t)$, and calculates its phase with respect to the demodulation signals. These pieces of information are conveyed by the H_d and H_q components in the figure.The LTI controller computes the control signals F_d and F_q

4

according to the references and the actual driving force is obtained by amplifying the modulated control by multiplying them by the same sinusoidal signals.

The demodulation reduces the requirements on the controller since low bandwidth compensators are sufficient. In [18], some properties of this strategy are studied under some assumptions. First, the poles of the demodulated system are shifted by $i\Omega$ to the ones of the original system, hence the less demanding requirement on the controller. Second, the delay of the original system are invariant with respect to the modulation and demodulation. Thus they affect the bandwidth of the demodulated system, but not the actual one. This implies that even rapidly oscillating systems can be regulated by slow controllers. The zeros might be affected in a more complicated way, but if the modulation frequency is large enough compared to the dynamic of the oscillator, they roughly behave in a similar manner as the poles.

Actually, in [16], the proposed method provides the equations of the demodulated before filtering. Assuming that the poles of $\eta^{(k)}$ are slow compared to Ω_k (the modulation angular frequency) and the bandwidth of the controller is small, one can write in complex polar form:

$$\underline{\eta}^{(k)}(t) = (H_d^{(k)}(t) + jH_q^{(k)}(t))e^{j\Omega_k t} \tag{5}$$

$$\underline{f}^{(k)}(t) = (F_d^{(k)}(t) + jF_q^{(k)}(t))e^{j\Omega_k t} \tag{6}$$

where $H_d^{(k)}$ and $H_q^{(k)}$ are respectively the real and imaginary part of the modal amplitude, $F_d^{(k)}$ and $F_q^{(k)}$ the real and imaginary part of the modal effort, Ω_k is the excitation frequency (k will later be the index to distinguish the various modulations). By replacing the Eq. (5), its derivatives and the Eq. (6) in the Eq. (2) a system of two differential equations is obtained which leads to:

$$\begin{aligned} \ddot{H}_d^{(k)} &= (\Omega_k^2 - \omega_k^2)H_d^{(k)} + 2\xi_k\Omega_k\omega_k H_q^{(k)} - 2\xi_k\omega_k\dot{H}_d^{(k)} + 2\Omega_k\dot{H}_q^{(k)} + F_d^{(k)} \\ \ddot{H}_q^{(k)} &= -2\xi_k\Omega_k\omega_k H_d^{(k)} + (\Omega_k^2 - \omega_k^2)H_q^{(k)} - 2\Omega_k\dot{H}_d^{(k)} - 2\xi_k\omega_k\dot{H}_q^{(k)} + F_q^{(k)} \end{aligned} \tag{7}$$

Unlike the model proposed in [19], the proposed model in Eq. (7) is written directly in an analytical form as a function of the modal parameters ξ_k, ω_k and the modulation/demodulation frequency Ω_k. By this way, a systematic approach for the controller design of a single mode has been proposed in [16], which is described in the next section.
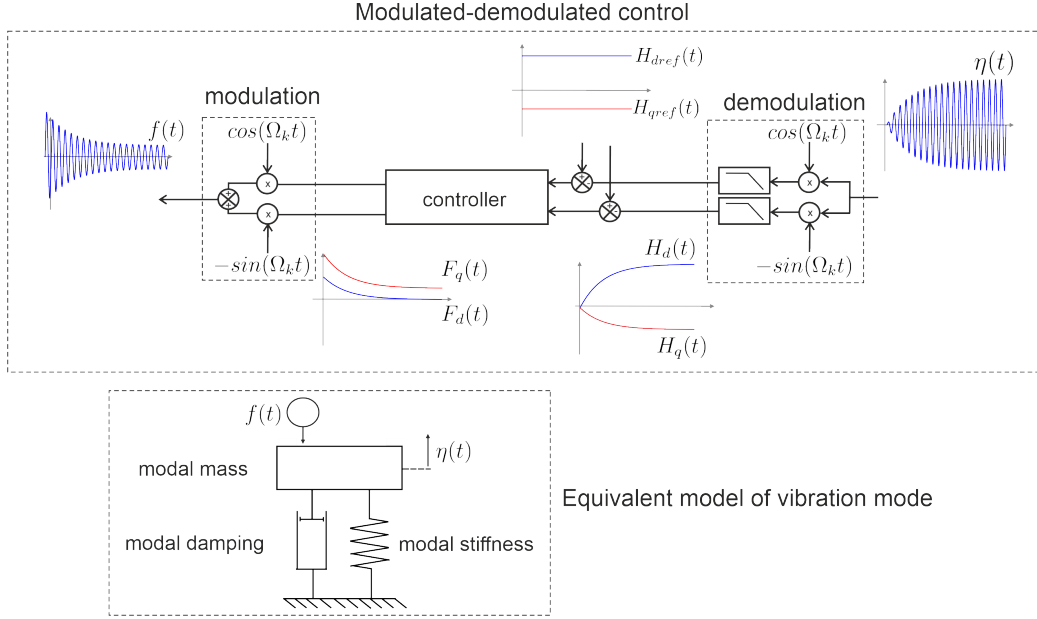
Figure 2: Principle of modulated-demodulated control (vector control) and the equivalent model of a single vibration mode, an example of the obtained waveforms is shown for each part of the modulated-demodulated control structure

2.3. Control in demodulated base

To design the controller ensuring zero steady-state error, the Eq. 7 are rewritten in a state space form, introducing two new states $\int H_d^{(k)} dt$ and $\int H_q^{(k)} dt$:

$$
\underbrace{\begin{bmatrix} H_d^{(k)} \\ H_q^{(k)} \\ \dot{H}_d^{(k)} \\ \dot{H}_q^{(k)} \\ \ddot{H}_d^{(k)} \\ \ddot{H}_q^{(k)} \end{bmatrix}}_{\dot{x}_k} = \underbrace{\begin{bmatrix} 0 & 0 & 1 & 0 & 0 & 0 \\ 0 & 0 & 0 & 1 & 0 & 0 \\ 0 & 0 & 0 & 0 & 1 & 0 \\ 0 & 0 & 0 & 0 & 0 & 1 \\ 0 & 0 & a_1 & a_2 & a_3 & a_4 \\ 0 & 0 & -a_2 & a_1 & -a_4 & a_3 \end{bmatrix}}_{A_k} \underbrace{\begin{bmatrix} \int H_d^{(k)} dt \\ \int H_q^{(k)} dt \\ H_d^{(k)} \\ H_q^{(k)} \\ \dot{H}_d^{(k)} \\ \dot{H}_q^{(k)} \end{bmatrix}}_{x_k} + \underbrace{\begin{bmatrix} 0 & 0 \\ 0 & 0 \\ 0 & 0 \\ 0 & 0 \\ 1 & 0 \\ 0 & 1 \end{bmatrix}}_{B_k} \underbrace{\begin{bmatrix} F_d^{(k)} \\ F_q^{(k)} \end{bmatrix}}_{u_k} \quad (8)
$$

where $a_1 = \Omega_k^2 - \omega_k^2$, $a_2 = 2\xi_k \Omega_k \omega_k$, $a_3 = -2\xi_k \omega_k$ and $a_4 = 2\Omega_k$. A Linear Quadratic Regulator is then used to design a state-feedback, which optimizes

6

the quadratic criterion [20]:

$$J_k = \int_0^\infty \left(x_k^T Q_k x_k + u_k^T R_k u_k \right) dt \tag{9}$$

The state-feedback $u_k = -K_k x_k$ is found by:

$$K_k = R_k^{-1} B_k^T P_k \text{ for } P_k \text{ s.t. } A_k^T P_k + P_k A_k - P_k B_k R_k^{-1} B_k^T P_k + Q_k = 0 \tag{10}$$

Following [16], particular weighting matrices Q_k and R_k are chosen:

$$R_k = \text{diag}(q_{ki}, q_{ki}, q_{kp}, q_{kp}, 0, 0) \tag{11}$$

$$Q_k = \text{diag}(1, 1) \tag{12}$$

which promote proportional-integral action, and treat symmetrically the closed loop dynamics of $H_d^{(k)}$ and $H_q^{(k)}$.

Along with this choice, it is specified that the close-loop step response should be as close as possible to the one of a first order. Moreover, in order to impose a $95\,\%$ closed-loop response time t_k', the ratio $\alpha_k = \frac{t_k}{t_k'}$ where t_k is the $95\,\%$ open-loop response time, is introduced in the LQR algorithm by letting:

$$q_{ki} = \left(2\alpha_k \xi_k^2 \omega_k^3 \right)^2 \tag{13}$$

$$q_{kp} = \left(2\alpha_k \xi_k \omega_k^2 \right)^2 \tag{14}$$

From a practical point of view, the resulting feedback control is modified into a MIMO-PID, which actually simplifies to a MIMO-PI in the case of a discrete implementation.

Finally to sum-up, Fig. 3 depicts the overall process from the point of view of the frequency spectra obtained at each steps when $\Omega_k = \omega_k$. At first, the velocity spectrum of the mode of interest is centered around $\mp\omega_k$. Once demodulated, the translation of the poles gives a first set of frequency centered around zero, and two lateral lobes centered at $\mp2\omega_k$ appear. They are filtered out and the bandwidth of the zero-centerd lobe is modified of the controller according to the value of α_k selected. In the last step, the modulation translates back the modified central lobe to ω_k.

2.4. Multimodal control

The design procedure discussed the bandwidth around the resonant frequency of a mode can be allocated. In order to control several modes, a

bank of controllers can be implemented in parallel as schematized in Fig. 4. Each path follows the principle developed for a single mode, the main difference being that each controller is tuned on a given frequency thanks to the modulation/demodulation frequency Ω_k. First, the measurement $w_s^{(m)}$ are combined linearly and then filtered with frequency filters in order to reconstruct each modal coordinate $\eta^{(k)}$. The modal coordinate is then demodulated which gives its real $H_d^{(k)}$ and imaginary $H_q^{(k)}$ component in its demodulated base. The controller calculates the modal forces components $F_d^{(k)}$, $F_q^{(k)}$ from the measurement $H_d^{(k)}$, $H_q^{(k)}$ and their respective references $H_{dref}^{(k)}$, $H_{qref}^{(k)}$. The components $F_d^{(k)}$ and $F_q^{(k)}$ are then modulated and give the modal forces $f^{(k)}$.

The proposed parallelization requires that the controllers are independent from each other i.e the influence of a given control effort $f^{(i)}$ on a kth mode ($i \neq k$) is negligible compared to $f^{(k)}$. this assumption imposes that the dynamic of a controller remains within a given bandwidth such that no overlappings between neighbour controllers occur. Such a set-up is depicted in the Fig. 3-e where the overall frequency response of the parallelized controller surrounds resonant frequencies of the selected modes without intersection. Moreover, no unwanted mode should lie within a controlled bandwidth. Similarly, the presence of a modal coordinate $\eta^{(i)}$ in the measurement of a kth mode ($i \neq k$) should negligible compared to $\eta^{(k)}$.

3. Experimental set-up

3.1. Hardware

3.1.1. Mechanical design

The proposed set-up is a an experimental prototype for a haptic feedback device that generates a localized tactile sensation on a touchscreen by modal superposition [22], while using piezoelectric transducers. It consists in a $150 \times 100 \times 2$ mm^3 glass plate onto which 34 piezoelectric monolayer patches (Noliac NC 51, $9 \times 5 \times 0.5$ mm^3) are glued. A patch possesses a folded electrode (cf Fig. 5-c) so according to the connection two different polarization can be chosen (since the glass plate defines no common ground). Behind the plate, a 5" LCD touchscreen is placed to later serve as a pointing and display device. To this end, the central area of the set-up must remain clear, which implies that the piezoelectric patches are confined at the periphery of the plate as illustrated in Fig. 5-b
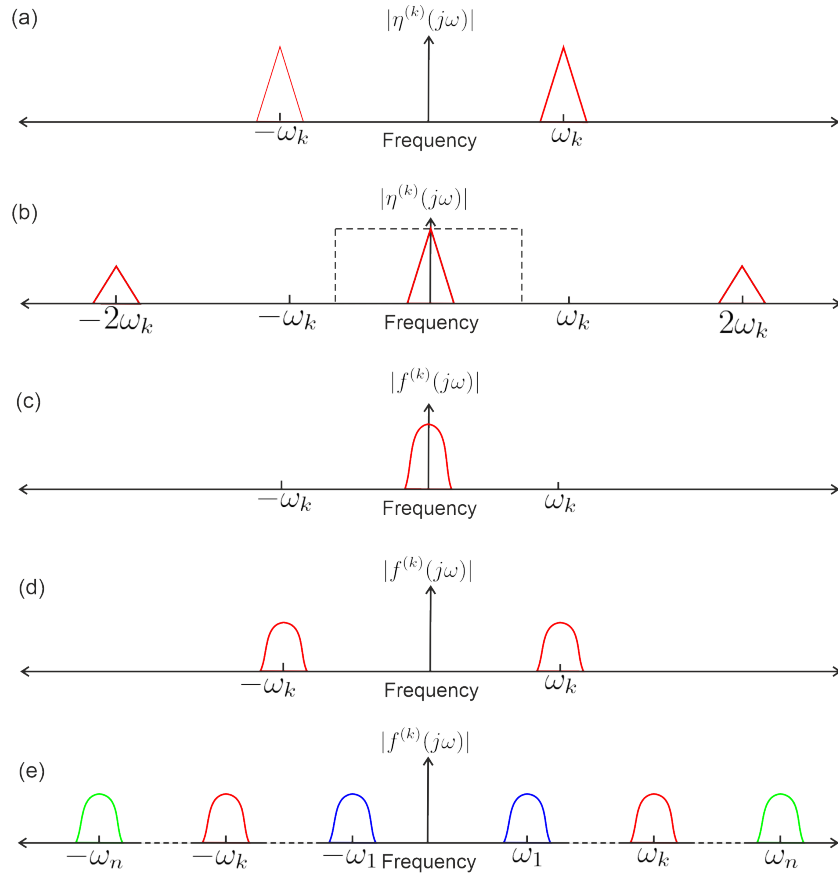
8

Figure 3: Conceptual overview of modulated-demodulated control in the case of multi-modal control,adapted from [21] : (a) Frequency spectrum of one modal coordinate, (b) Frequency spectrum after demodulation the measured modal coordinate, (c) synthesis of the controller in the demodulated base, the bandwidth of the controller is represented in dashed lines, (d) modal control signal after modulation, and (e) Resulted spectrum of the control efforts after superposing n modulated-demodulated controllers, each color correspond to the control signal of a single mode.

The finger acts as a perturbation that damps the vibrations [23, 24]. Therefore, the feedback control is needed to ensure a repeatable tactile stimulation independently of the finger mechanical properties and the pressure applied. Lastly, the vibration amplitude should be large enough to be detectable. This implies that the ceramics must transfer enough energy to the modes. Due to the limited number of patches, and since the applied voltages must respected the specifications of the manufacturer, the set of available
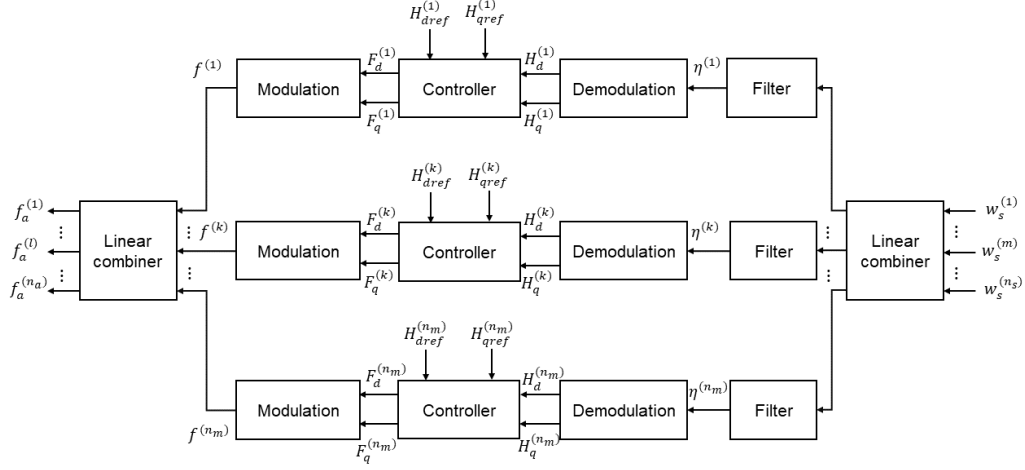
Figure 4: Proposed control structure, composed by modal filters and parallelization of n_m modulated-demodulated controllers.
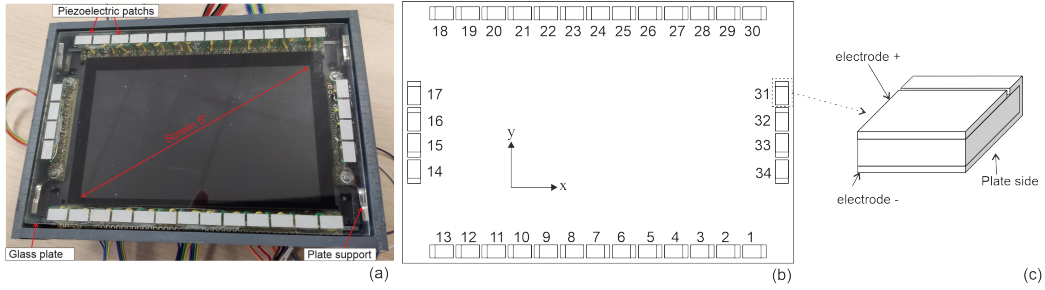

Figure 5: (a) Picture of the experimental device; (b) Location of the piezoelectric patches; (c) Schematic of a piezoelectric patch.

ceramics must be carefully divided into subsets assigned to the modes.

To do so, the later must be known then selected according to the desired velocity fields that should be synthesized. For this purpose, the Eq. 3 is adapted to the specificity of the piezoelectric actuators as they do not produce concentrated forces, but as a combination of forces and moments. They results from the piezoelectric contribution to the stresses at the boundary of a ceramic thus both their shape and location with respect to a mode shape matter [preumont]. The modal force developped by a ceramic i is calculated by [Ehsan]:

$$f_a^i = e_{31}d \oint_{\partial\Gamma_i} \nabla\mathbf{\Psi}^{(k)}.\mathbf{n}d\Gamma V_i = \Phi^{k,i}V_i \qquad (15)$$

10

where e_{31} [N V^{-1}] is the piezoelectric coefficient, d is the distance between the patch and the plate mid-planes and V_i is the applied voltage.
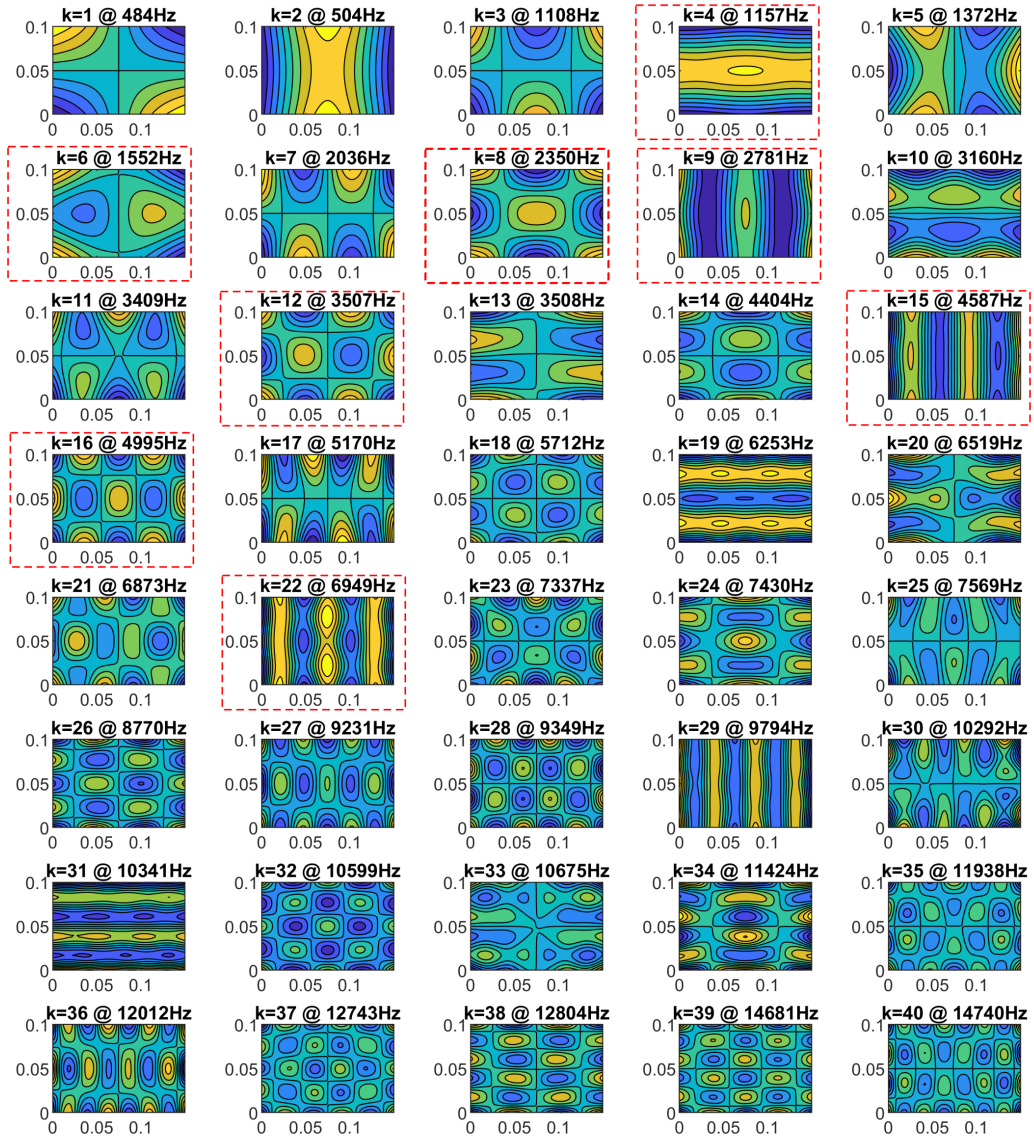

Figure 6: The first forty mode shapes of the plate and the corresponding resonance frequencies, the selected modes are surrounded in dashed red lines.

To estimate the global piezoelectric coefficient $\Phi^{k,i}$, the mode shape were approximated using the Rayleigh-Ritz method [25, 26] where the assumed modes are free-free beam modes. These approximation were then used to estimate coupling between a patch and a mode. the first forty mode shapes and their resonant frequencies are shown in Fig 6. In Fig. 7-a the estimated normalized $\phi^{(k,i)}$ are represented as a matrix. A square defines the coupling between a patch and a mode. It can be interpreted in two ways: spanning the rows vertically at a given columns (i.e a given patch) quantifies the efficiency of the patch to energize the modes, while spanning the columns gives the ceramics prone to excite a given mode. Note that due to the reversibility of piezoelectricity, $\phi^{(k,i)}$ also relates the electrical charge induced by a deformation, thus the same representation also indicates the ceramics that can be used as sensors.
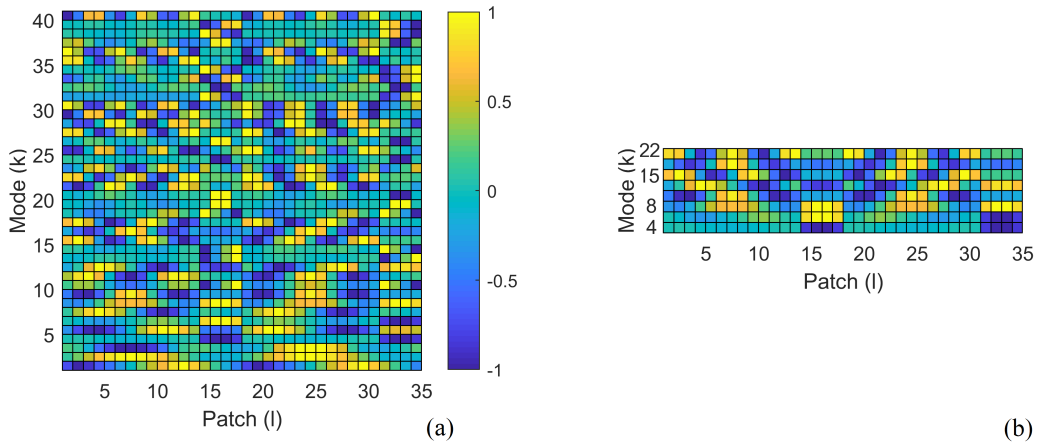

(a)   (b)

Figure 7: (a) Normalized modal coupling matrix $\mathbf{\Phi}$, where each case correspond to a modal coupling gain $\phi^{k,l}$, (b) normalized modal coupling matrix $\mathbf{\Phi}(\mathbf{E})$ associated with the set of selected modes $E = \{4, 6, 8, 9, 12, 15, 16, 22\}$.

3.1.2. Electronic

The control unit is composed of a set of Digital Signal Processor (DSP) STM32F4 (STMicroelectronics) as shown in the Fig. 8.The first DSP is principally responsible for the communication with a computer on a USB link. This allows to program the other DSP, send them references, parameters and gather measurements. Moreover, it provides a common clock signal to ensure the synchronization of the controllers. The communication between the DSP

is performed through a SPI (Serial Peripheral Interface) link. The DSP 2 and 3 implement two controllers each. The modulated control signal is amplified by two half-bridge DC to AC converter from a $100\,V$ DC bus using a $500\,kHz$ pulse width modulation (PWM). The PWM voltages are then filtered by passive low pass RLC circuits before supplyning the ceramics. In the design of Fig. 5 some ceramics will be used as actuators, the rest as sensors.

The ST32F4 has up to three Digital to Analog Converters (DAC), which limits to three measurements available to a set of two controllers. This is a strong constraint, and thus a method to select the ceramics assigned for measurements ans actuation is necessary. Unfortunately, it is not anymore possible to use model reduction [1] or controllability of observability gramians [27, 28]. Specific selection methods must be defined.
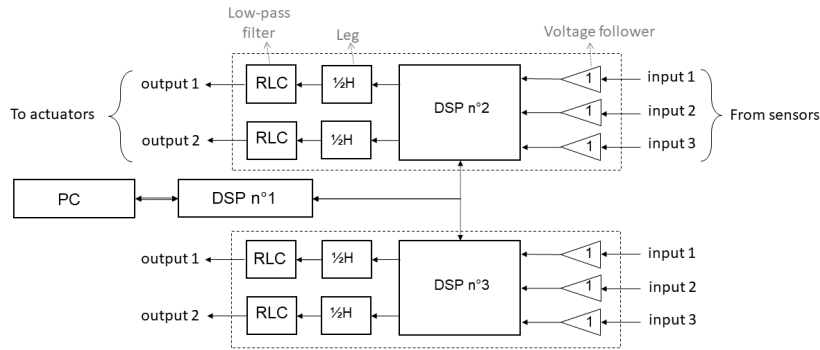

Figure 8: Structure of the control unit, composed with a set of DSP controllers, each DSP possess its own measurement inputs and control signals outputs

3.2. Protocol

3.2.1. Reference

The prototype is limited to the simultaneous control of four modes. In the following experiments though, eight modes will be used, repeating the focusing with four modes at each run, then reconstructing the velocity field. This approach holds because of the linearity and because the electronic guarantees the synchronization of DSP. However, a reference velocity field composed of eight mode must be defined. In this work, a sinc is chosen since it is known that number of harmonics is limited and it can easily controlled. We thus

define an ellipsoidal spatial sinc velocity reference by:

$$\dot{w}_f^*(x,y) = \dot{w}_{ref}^* \operatorname{sinc} \frac{(x-x_0)^2 + a_s(y-y_0)^2}{R_s^2} \qquad (16)$$

where $\dot{w}_{ref}^*$ defines the peak amplitude, $\{x_0, y_0\}$ its location, and R_s, a_s adjust the ellipsoid. Here $a_s = 0.5$ and $R_s = 40$ mm and three focusing location are defined as in Fig. 9.

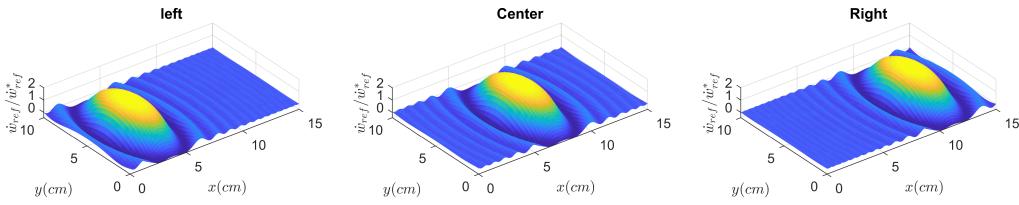Once the reference defined, the modal velocity references are computed by

Figure 9: Velocity fields references: the center of the main lobes are located at $(37.5\text{mm}, 50.0\text{mm})$, $(75.0\text{mm}, 50.0\text{mm})$ and $(112.5\text{mm}, 50.0\text{mm})$ in order to focus at the left, center and the right of the plate respectively.

a modal projection, that is:

$$\dot{\eta}_f^{*(k)} = \iint_{S_p} \psi^{(k)}(x,y)\dot{w}_f^*(x,y)dxdy \qquad (17)$$

where S_p is the surface of the plate. The $\dot{\eta}_f^{*(k)}$ define the reference values to be reached at the time of focusing and are represented in Fig. 6 for the 40 modes. It can be observed that they participate unevenly and therefore the decomposition can be pruned to retain only eight modes. To do this the τ criterion defined in [13] is adapted. Denoting E the subset of selected modes ($\dim E = 8$), the criterion is written for the set of modes (cf Fig.) as follows

$$\tau = \left(\frac{\displaystyle\sum_{k \in E} (\dot{\eta}_f^{*(k)})^2}{\displaystyle\sum_{k=1}^{n_m} (\dot{\eta}_f^{*(k)})^2} \right)^{1/2} \qquad (18)$$

Evaluating τ over all combinations finally gives $E = \{4, 6, 8, 9, 12, 15, 16, 22\}$ with $\tau-$scores 89%, 97% and 89% for the left, center and right location
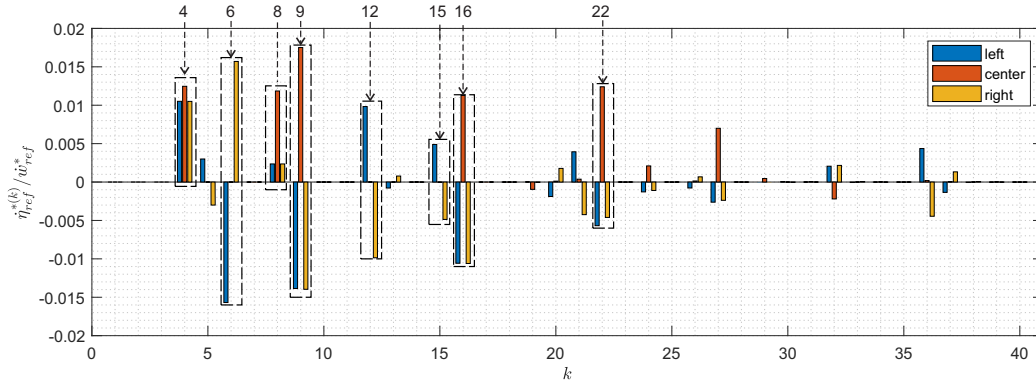
14

Figure 10: Modal participation factors for each spatial reference : left, center, right, the selected modes are surrounded in dashed lines
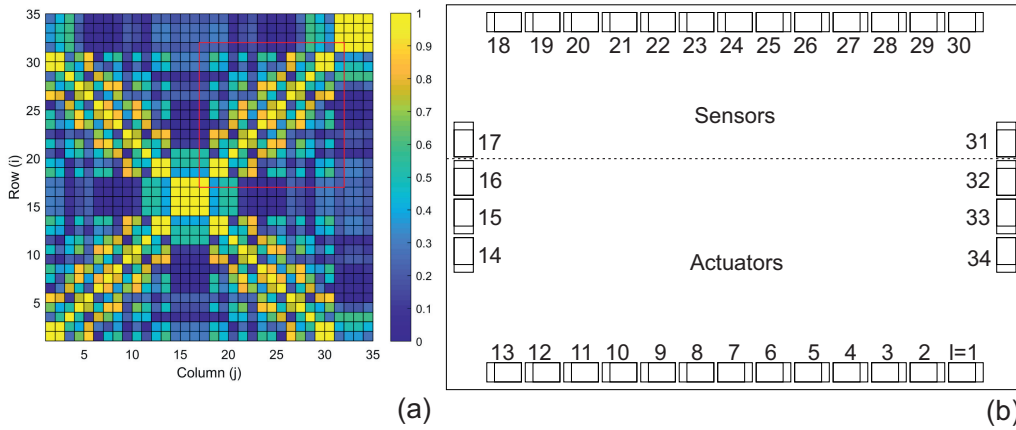

Figure 11: (a) Orthogonality of the coupling vectors in the case of the selected modes ; (b) Sensors and actuators sets

respectively (cf. Fig 10).

In Fig. 7-b, the sub-matrix $\Phi(E)$ which gathers the piezoelectric force factor $\Phi^{k,i}$ for the set E is represented. Then the matrix $\left|\Phi(E)^T\Phi(E)\right|$ is computed to evaluate the redundancy in the coupling of the ceramics with respect to the modes. It is then normalized so as to have a unity diagonal, hence measuring the correlations of the ceramics and the modes (cf. Fig. 11-a). To select a set of actuators prone to energize a mode, one should choose ceramics with high correlation along a row or a column. On the contrary, ceramics with low covariance indicate complementary information in the measurements that facilitates the recovery of modal coordinates.

15

Finally to avoid electromagnetic compatibility issues observed in previous works, two separated areas are assigned to actuators and sensors (cf. Fig. 11-b) these regions corresponds to the red rectangle outlined in Fig. 11-a.

3.2.2. Actuators

In order to control a mode $k \in E$, a subset of ceramics within the set of actuators of Fig. 11-b must be defined. A trade-off between a strong coupling assigned to the mode and a weak coupling with the other mode must be found to realize a modal filtering. To do so, let $\boldsymbol{\phi}_a^{(k)}$ be the vector which i-th component is $\phi_a^{(k,i)}$, and introduce the connection vector $\boldsymbol{p}$ which components take values in $\{-1, 0, 1\}$. A zero component means no connection, while ± 1 indicates a connection, the sign being chosen relative to the connection of the ground of the supply with respect to the polarization of the ceramic. The following criterion is introduced:

$$S_k(\boldsymbol{p}) = \left| \boldsymbol{p}^T \boldsymbol{\phi}_a^{(k)} \right| - c_p \sum_{\substack{k'=1 \\ k' \neq k}}^{n_m} \left| \boldsymbol{p}^T \boldsymbol{\phi}_a^{(k)} \right| \tag{19}$$

Let $\mathcal{P}_n$ be the set of all exclusive and distinct connections vector $\boldsymbol{p}$ with n connections. By that, we mean that two vectors in $\mathcal{P}_n$ have no common non-nil component, and there are no opposite vector because it would actually be the same connection if the voltage polarity is reversed. Then the aim is to find four vectors $\boldsymbol{p} \in \mathcal{P}$ such that the worst case is minimized, that is the solution $\hat{\mathcal{P}}_n$ in the set of selected modes $\mathcal{M}$ is:

$$\hat{\mathcal{P}}_n = \max_{\mathcal{P}_n} \min_{\substack{k \in \mathcal{M} \\ p \in \mathcal{P}_n}} S_k(\boldsymbol{p}) \tag{20}$$

In this way, the connections will ensure that the voltage range is used at best, and thank to the parameter c_p the design can be tuned against spill-over. The problem is non convex and discrete: in this work it was solved by brute force.

16

3.2.3. Mode measurements

The measurements are given by a superposition of modal coordinate, pondered by the piezoelectric effects :

$$
\underbrace{\begin{bmatrix} w_s^{(1)} \\ \vdots \\ w_s^{(n_s)} \end{bmatrix}}_{\mathbf{w_s}} = \underbrace{\begin{bmatrix} \phi_s^{(1,1)} & \cdots & \phi_s^{(1,n_m)} \\ \vdots & \ddots & \vdots \\ \phi_s^{(n_s,1)} & \cdots & \phi_s^{(n_s,n_m)} \end{bmatrix}}_{\mathbf{\Phi_s}} \underbrace{\begin{bmatrix} \eta^{(1)} \\ \vdots \\ \eta^{(n_m)} \end{bmatrix}}_{\mathbf{h}}
\tag{21}
$$

where, again, the coefficient $\phi_s^{(m,k)}$ depends on the position of the sensor with respect to a given mode. Therefore a sensor provides a weighted superimposition of modes.

The usual approach consists in applying a Penrose-Moore pseudo-inverse to get $\hat{\boldsymbol{h}} = \boldsymbol{\Phi}_s^\dagger \mathbf{w}_s$. However, as mentioned earlier, the reduced number of measurement available (three measurement for two modes) is challenging. Here, a combined spatial/frequency filtering is applied. Consider the schematic of Fig 4. The estimates is given by

$$
\hat{\eta}^{(k)}(s) = G_{eq}^{(k)}(s) \left(\begin{bmatrix} d^{(k,1)} \\ \vdots \\ d^{(k,n_s)} \end{bmatrix}^T \begin{bmatrix} \phi_s^{(1,1)} & \cdots & \phi_s^{(1,n_m)} \\ \vdots & \ddots & \vdots \\ \phi_s^{(n_s,1)} & \cdots & \phi_s^{(n_s,n_m)} \end{bmatrix} \right) \begin{bmatrix} \eta^{(1)}(s) \\ \vdots \\ \eta^{(n_m)}(s) \end{bmatrix}
\tag{22}
$$

where $d^{(k,m)}$ is the row of the matrix $\boldsymbol{D}$ representing the gain of the linear combiner associated with the sensor m and the mode k, $G_{eq}^{(k)}(s)$ is the equivalent transfer function of the frequency filter in cascade with the demodulation operator (Fig. 4) which has its own frequency response depending of the used demodulation technique [29].

To simplify the procedure, the frequency filter is introduced into $\boldsymbol{\Phi}_s$. Then defining the gains of the filter for each modes frequencies $G_{eq}^{(k,i)} = \left| G_{eq}^{(k)}(j\omega_i) \right|$, one has:

$$
\hat{\eta}^{(k)}(s) = \begin{bmatrix} d^{(k,1)} \\ \vdots \\ d^{(k,n_s)} \end{bmatrix}^T \begin{bmatrix} \phi_s^{(1,1)} G_{eq}^{(k)}(s) & \cdots & \phi_s^{(1,n_m)} G_{eq}^{(k)}(s) \\ \vdots & \ddots & \vdots \\ \phi_s^{(n_s,1)} G_{eq}^{(k)}(s) & \cdots & \phi_s^{(n_s,n_m)} G_{eq}^{(k)}(s) \end{bmatrix} \begin{bmatrix} \eta^{(1)}(s) \\ \vdots \\ \eta^{(n_m)}(s) \end{bmatrix}
\tag{23}
$$

and thus the vector of linear combiner $\mathbf{d}^{(k)}$ is calculated as follow :

$$
\mathbf{d^{(k)}} = \boldsymbol{\Delta}^{(\mathbf{k})} \boldsymbol{\Phi}_{\mathbf{sf}}^{(\mathbf{k})\dagger}
\tag{24}
$$

17

where $\mathbf{\Delta^{(k)}} = \begin{bmatrix} \delta_1^k & \ldots & \delta_i^k & \ldots & \delta_{n_m}^k \end{bmatrix}$ is a selection vector and δ_i^k correspond to Kronecker delta. The procedure is iterated for the various filter, and each time the corresponding line of $\boldsymbol{D}$ is updated.

The procedure is valid for one sensor connection. Therefore, an optimisation procedure similar to the previous one is implemented to iterate on the set of possible connections. A constraint is added to the procedure in order to avoid the measurement noise amplification, which is induced by a rank deficiency of the matrix $\mathbf{\Phi_{sf}^{(k)}}$ [30]. The constraint consists in penalizing a great values of the linear combiner $\mathbf{d^{(k)}}$.

3.2.4. System Calibration

The plate mode-shapes identification is done by using a laser vibrometer (Polytec PSV-400) and while exciting a given set of actuators. From the spatio-frequency response of the plate, the mode shapes are extracted using a peak picking method. In the Fig. 12 are superposed the theoretical (Rayleigh-Ritz) mode shapes and the experimentally identified one. it can be observed that the experimentally identified mode shapes match well with the predicted one using Rayleigh-Ritz method. However, due to the influence of the PZT patches and the connecting wires, the resonance frequencies are around 12% lower than the calculated frequencies (Fig.6).
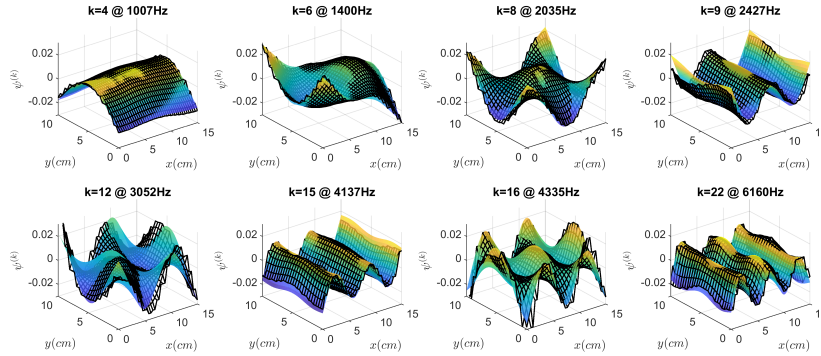

Figure 12: Mode shapes of the selected modes identified experimentally (black grid) and the theoretical one (colored surface).

The identified resonance frequencies ω_k and modal damping ξ_k are summarized in the Table 1. The identification procedure consists in a frequency sweep around the resonance frequency of given controlled mode by using the associated sensors and actuators. The modal parameters are extracted using

18

the quadrantal frequencies method as explained in [16]. It can be observed that all the controlled modes are lightly damped $\xi_k < 0.01$ (1%).

Mode	4	6	8	9	12	15	16	22
Frequency (Hz)	1007	1400	2035	2427	3052	4137	4335	6160
Damping (%)	0.45	0.31	0.45	0.54	0.88	0.48	0.69	0.61

Table 1: Identified parameters

4. Results

Considering the limitation of the experimental set-up, only four modes can be controlled simultaneously. Therefore, we propose to divide the experiment in two parts, in each part we control four vibration modes and we adapt the experimental implementation adequately. Since the system is linear and assuming that there is no coupling between the modal coordinates, then the superposition of both results is equivalent to the result obtained by exciting simultaneously all of the eight selected modes.

The first part of the experiment consists in exciting the modes $\{4, 8, 16, 22\}$ that have a high contribution factors for a 'center' focus. First, we validate the proposed control approach for a 'center' focus by superposing the modes $\{4, 8, 16, 22\}$. Secondly, we show the results obtained by exciting successively the modes $\{4, 8, 16, 22\}$ and then the modes $\{6, 9, 12, 15\}$, for a 'left', 'center' and 'right' focus of the velocity field.

4.1. Actuation

By taking a penalty factor $c_p = 1.5$ in the criterion (19) the result of the actuators selecting procedure with the modes $\{4, 8, 16, 22\}$ is represented in the Fig. 13, where each color corresponds to a mode, the sign $+/-$ represents the power polarity of each actuator.

In order to validate the actuators selecting procedure of the section 3.2.2, the time and frequency responses of each controlled mode are analysed. If we consider that a vibration mode excited at its resonance is a linear lightly damped harmonic oscillator (second order system), then its time step response in its demodulated base should be a convergent exponential and its frequency response (Nyquist diagram) should form a circle in the complex plan [31]. If a neighbor mode is excited and measured, its influence could be observed in the time and frequency response.
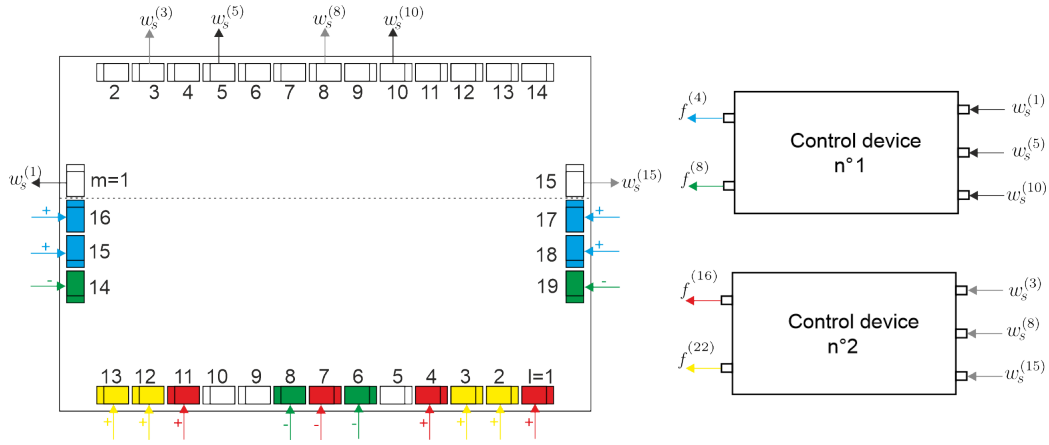
19

Figure 13: Connection scheme of the sensors and the actuators to the control devices, the sign +/− represents the power polarity of each actuator.
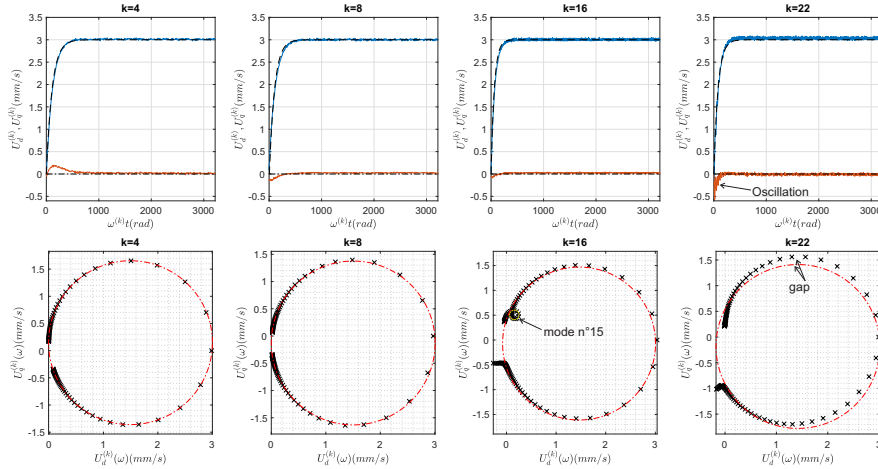

Figure 14: Time (top) and frequency (bottom) responses in the demodulated bases, with an isolated excitation. the blue and red curves in the time responses correspond respectively to $U_d^{(k)}$ and $U_q^{(k)}$. The red curves in the frequency responses correspond to the identified circles

The Fig. 14 shows the time and frequency responses of the selected modes in their demodulated bases, when each mode is excited separately at their respective resonance frequencies and the modal force are taken so as to obtain the same modal velocity amplitude. The modal velocity is written as

its complex form as follow:

$$\underline{u}^{(k)}(t) = \underline{\dot{\eta}}^{(k)}(t) = (U_d^{(k)}(t) + jU_q^{(k)}(t))e^{j\Omega_k t} \tag{25}$$

where $U_d^{(k)}$ and $U_q^{(k)}$ are respectively the real and imaginary part of the modal velocity and they can be approximated as $U_d^{(k)} = \Omega_k H_q^{(k)}$ and $U_q^{(k)} = -\Omega_k H_d^{(k)}$. It can be established that the response of the $U_d^{(k)}$ component matches with the response of a first order system [16]. The component $U_q^{(22)}$ shows some oscillations at the beginning of the transient. These oscillations are due to the excitation of a neighbour mode by a spillover effect whose influence is visible by a gap in the frequency response. The consequence of this spillover is presented in the next section.

4.2. Sensors

The first step for the measurement process establishment is to define the demodulation bloc and the frequency filter forms. The demodulation bloc consists in a moving average method [29] [10] with a window of two oscillation periods $T_k = 4\pi/\omega_k$. The additional frequency filter is a second order band-pass filter which writes :

$$G_{pb}^{(k)} = \frac{2\xi_{bp}\omega_k s}{s^2 + 2\xi_{bp}\omega_k s + \omega_k^2} \tag{26}$$

where $\xi_{bp} = 0.42$ defines the filter bandwidth. The chosen value is a good compromise between the selectivity of the filtering process and the phase shift induced.

By considering the frequency response of the equivalent frequency filter, the results of the selecting procedure is summarized in Fig. 13. The sensors associated with the 4th and 8th modes are $\{1, 5, 10\}$ and those associated with the 16th and 22th modes are $\{3, 8, 15\}$. The corresponding normalized spatial filters are shown in the Fig. 15, the null rows represent unused sensors.

In order to validate the calculation method for the modal filter weighting gains $d^{(k,m)}$, the filtering process is simulated for the case of the sensors/modes combination shown in the Fig. 13. The first calculation method is the classical one and the second method is the proposed one Eqs. (24). The modes are excited simultaneously at their respective resonance frequencies and the modal force are taken so as to obtain the same modal velocity amplitude. The modal responses in the respective demodulated base are
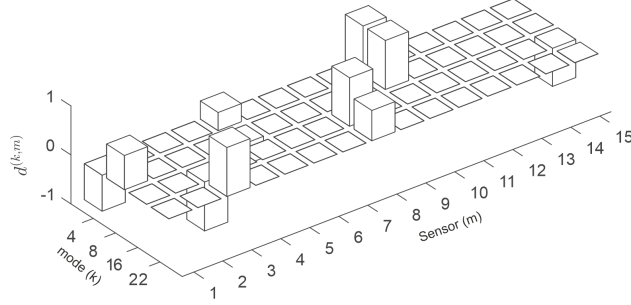
21

Figure 15: Normalized Spatial filter gains $d^{(k,m)}$.

shown in the Fig. 16.a for the classical method case and Fig. 16.b for the proposed method case. It can be observed that for some modes as the 22th one, the classical calculation method is sufficient to obtain a good measurement. However, in the case of the 8th the proposed method reduces the measurement residues by around 2.5 times while using the same sensors.
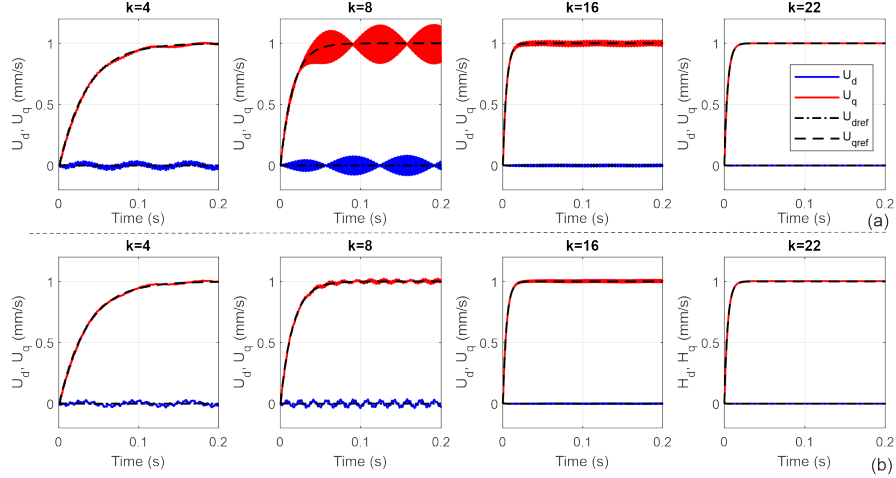

Figure 16: Obtained simulation responses with the classical (a) and the proposed (b) method for calculating the modal filter weighting gains, U_{dref} and U_{qref} correspond the ideal modal responses

After implementing the filtering and modulation-demodulation algorithm in the micro-controllers, the modes are excited simultaneously in open loop at their respective resonance frequencies with a step of voltage in the d-axis (real) and so as to obtain the same velocity amplitude. the influence of the modal filter on the measurement is shown in the Fig. 17. The Fig. 17.a shows

22

the obtained responses without spatial and frequency filters, in this case only a demodulation operation is applied on arbitrary sensor. The Fig. 17.b shows the responses obtained when applying the proposed combination of spatial and frequency filtering. It can be observed that due to the demodulation characteristic some measurement contains a small percentage of residues as for the 4th or 8th. The integration of spatial and frequency filters enhances the measurement and reduces drastically the residues, which can be observed principally for the 22th mode.
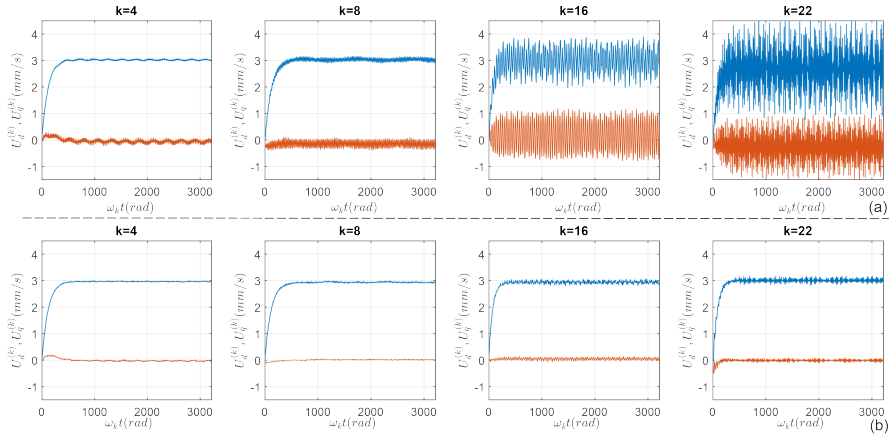

Figure 17: Influence of the modal filter on the measurement of the modal velocities, $U_d^{(k)}$ in blue and $U_q^{(k)}$ in red : (a) measurement responses by using only the demodulation bloc with an arbitrary sensor ; (b) measurement modal velocities while applying the proposed spatial frequency filter

4.3. Closed loop control

In this chapter, the closed loop control of several modes is presented. The proposed methodology is based on the controller design discussed in 2.3 which has been validated by Kaci & al. [16] for the case of controlling a single mode. The transition to the control of several modes is done thanks to the control structure shown in the Fig. 4 which allows to have an independent control for each mode.

From the modal parameters of the Tab. 1 and the controller design method described in 2.3, it is possible to calculate the Multi-Inputs-Multi-Outputs Proportional-Integral (MIMO-PI) controller gains, for each mode, while imposing a desired acceleration factor α_k. As a reminder, the acceleration factor is defined as the ratio of the open loop response time by the

closed loop one, $\alpha_k = 1$ results an equivalent closed loop dynamic than the open loop one.

In order to show the robustness of the proposed approach, different dynamics $\alpha_k = \{0.5, 1, 2\}$ are imposed and the closed loop time responses are recorded. The choices $\alpha_k = \{0.5, 1, 2\}$ translate respectively a slower, equivalent and faster closed loop dynamic than the open loop one, and each imposed acceleration factor α_k results different controller gains. The modal velocities references are taken $U_{dref}^{(k)} = 3\,\mathrm{mm\,s^{-1}}$ and $U_{qref}^{(k)} = 0$ and all of the four modes are excited simultaneously at their respective resonance frequencies.
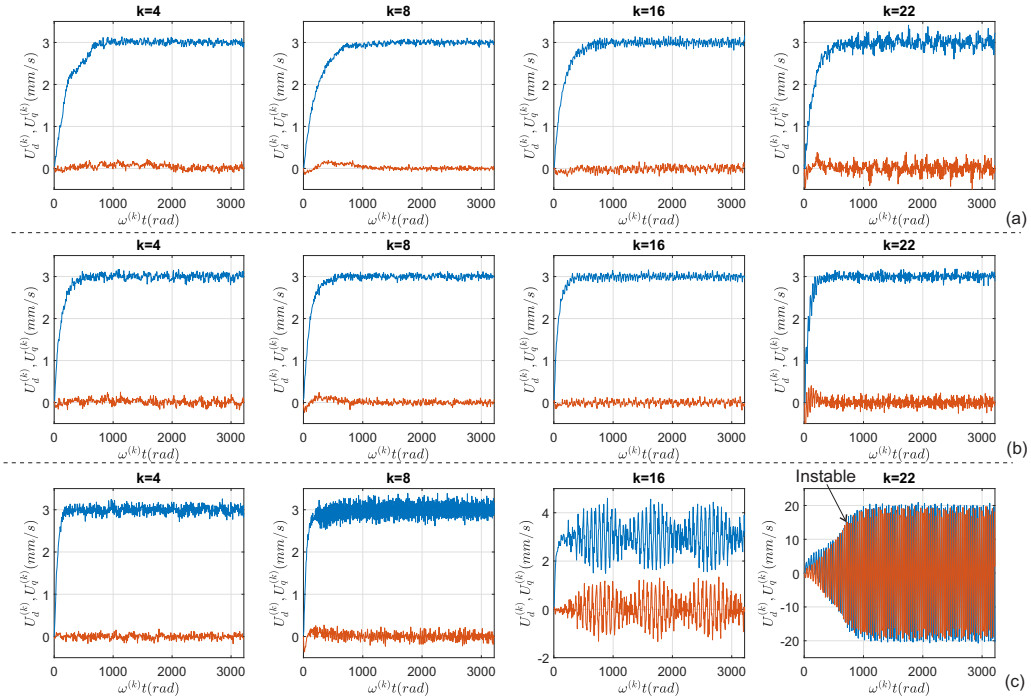

Figure 18: Closed loop time responses of the selected modes $k = \{4, 8, 16, 22\}$, for a simultaneous excitation, $U_d^{(k)}$ in blue and $U_q^{(k)}$ in red, (a) $\alpha_k = 0.5$, (b) $\alpha_k = 1.0$, (c) $\alpha_k = 2.0$

The obtained closed loop responses are shown in the Fig. 18. In the case where $\alpha_k = 0.5$ and $\alpha_k = 1$ all the four modes are stable, where their measurement shows low oscillations and all the modal references are reached despite of the simultaneous excitation of several modes. However, in the case where $\alpha_k = 2$ (Fig 18.c) the 22th is unstable which results in high oscillation in both d-q axis, these oscillations are limited by the maximum voltage that

can be generated by the control device. This instability can be explained by a large presence of the 24th whose the influence is visible in the gap on the frequency response Fig. 14.

4.4. Wave focusing

In a previous study Enferad & al. [13] generated focused waves by controlling several modes in open loop at their resonance frequencies. In this work, the modes are controlled in closed loop by using the proposed control structure in order to produce and adapt in real time the control effort. The modal references are defined as follow :

$$\dot{\eta}^{*(k)}(t) = \dot{\eta}_f^{*(k)} \cos(\omega_k(t - t_f)) \, \mathrm{e}^{\kappa_k \xi_k \omega_k |t - t_f|} \tag{27}$$

where $\dot{\eta}_f^{*(k)}$ is the modal velocity reference at the focusing time and calculated from the projection in Eq. (17), κ_k is an acceleration factor of the reference which allows to adjust the transient of each mode. The reference formula (27) correspond to the response of an unstable mode $\xi_k < 0$ for $t \le t_f$ and to the response a stable mode $\xi_k > 0$ for $t > t_f$. The reference is composed by harmonic vibration $cos(\omega_k(t - t_f))$ and an envelop $(\dot{\eta}_f^{*(k)} \, \mathrm{e}^{\kappa_k \xi_k \omega_k(t - t_f)})$ in the other side. The velocities references in the demodulated bases are calculated by writing the Eq. (27) in its complex form :

$$\underline{u}^{*(k)}(t) = \underline{\dot{\eta}}^{*(k)}(t) = \left(U_{dref}^{(k)}(t) + j U_{qref}^{(k)}(t) \right) \mathrm{e}^{j\omega_k(t - t_f)} \tag{28}$$

which gives after identification in the real and imaginary complex axis :

$$\begin{aligned} U_{dref}^{(k)}(t) &= \dot{\eta}_f^{*(k)} \, \mathrm{e}^{\kappa_k \xi_k \omega_k |t - t_f|} \\ U_{qref}^{(k)}(t) &= 0 \end{aligned} \tag{29}$$

thus, the amplitude and phase control is perfomed by the control of the components U_d and U_q. The carrier $\mathrm{e}^{j\omega_k(t - t_f)}$ possesses a non-null initial angle $-\omega_k t_f$ which ensures the synchronisation of the modal velocities at $t = t_f$. The modal amplitudes references are calculated by the variable change $H_{dref}^{(k)} = U_{qref}^{(k)}/\omega_k$ and $H_{qref}^{(k)} = -U_{dref}^{(k)}/\omega_k$.

Considering the dynamical nature of the reference signals, it is necessary to include in the control structure a reference tracking method which consist in a model-based feed-forward controller which is written in the discrete form:

$$\begin{bmatrix} F_d^{(k)}(z) \\ F_q^{(k)}(z) \end{bmatrix} = \mathbf{C_{ff}^{(k)}} \begin{bmatrix} H_{dref}^{(k)}(z) \\ H_{qref}^{(k)}(z) \end{bmatrix} \tag{30}$$
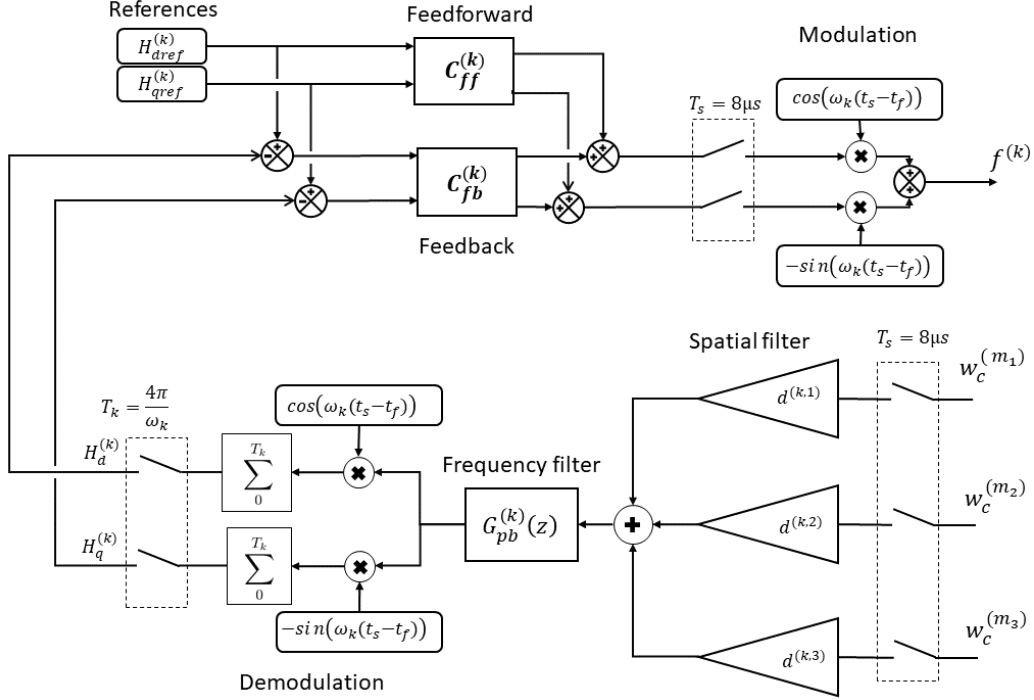
25

Figure 19: Control structure for one vibration mode

where $\mathbf{C_{ff}^{(k)}}$ is the discrete feedforward transfer function matrix.

The implemented control structure for one vibration mode is shown in Fig. 19. It consists in a measurement processing bloc which includes a spatial filter, a frequency filter and a demodulation operator. The carriers angles are initialized to $-\omega_k t_f$ in order to synchronize their angle at the focusing time t_f, t_s corresponds to the discretized time at $125\,\text{kHz}$ ($8\,\text{µs}$). The modal amplitude components $H_d^{(k)}$ and $H_q^{(k)}$ are controlledwith a sampling period of $T_k = 4\pi/\omega_k$. It means that the control efforts are updated each second vibration period of the controlled mode. $\mathbf{C_{fb}^{(k)}}$ corresponds to the transfer matrix of the MIMO-PI feedback controller described in section 2.3. The outputs of the controller $F_d^{(k)}$ and $F_q^{(k)}$ are modulated which results the modal effort $f^{(k)}$.

The first experiment consists in a focusing at the center of the plate by exciting four modes $(4, 8, 16, 22)$. The chosen velocity reference at the focusing point is $w_{ref}^* = 12\,\text{mm}\,\text{s}^{-1}$ which results after projection, to the modal velocities references $\eta_f^{*(k)}$ summarized in the Table.2. The shape of the

26

Mode (k)	4	8	16	22
$\dot{\eta}_f^{*(k)}$ (mm s^{-1})	3	3.72	3.36	2.04
κ_k	2	1.5	1	0.5
α_k	4	3	2	1

Table 2: Modal velocities references at the focusing time $\dot{\eta}_f^{*(k)}$, acceleration factor of the reference $\kappa^{(k)}$ and acceleration factor for the closed loop dynamic $\alpha^{(k)}$, for each controlled mode k

transients are imposed by the focusing duration t_f and by the acceleration coefficients κ_k associated with the references envelop $\dot{\eta}_f^{*(k)}e^{\kappa_k \xi_k \omega_k (t-t_f)}$. In order to reduce the transient duration, the coefficient κ_k is taken all the smaller as the rank of the mode is low. Concerning the closed loop dynamics α_k, it has been found experimentally that $\alpha_k = 2\kappa_k$ is a good compromise between disturbance rejection and noise amplification. We define the focusing time as $t_f = 131.1$ ms and the chosen coefficients κ_k and α_k are resumed in the Table.2.

The proposed control structure is validated by comparing the obtained results with and without feedback control (respectively with $\mathbf{C_{ff}} + \mathbf{C_{fb}}$ and just with $\mathbf{C_{ff}}$), in the presence and absence of external perturbation. In this case, the perturbation is a finger pushing around the center of the plate with a constant force. The obtained results are shown in Fig.20. In absence of feedback control, the Fig.20.a shows the sensitivity of the system if the modes are not exactly excited at their resonance frequency $\omega \neq \omega_k$, which can be observed in the $U_q^{(k)}$ components that are not null during the transient. The influence of the finger is also visible on the same figure, with an attenuation of $U_d^{(k)}$ components of the 4th and 8th mode principally. Since only feedforward control $\mathbf{C_{ff}}$ is used, the voltage in Fig.20.b does not depend on the measurement but just on the references. The ripples visible on the same figure are due to the numerical round-off which are all the greater as the resonance frequency is high. The integration of feedback controller (Fig.20.c) substantially reduces the tracking errors of both components $U_d^{(k)}$ and $U_q^{(k)}$. The associated voltages $V_d^{(k)}$ and $V_q^{(k)}$ are shown in Fig.20.d.

The modal velocities $\dot{\eta}^{(k)}$ in the natural bases are extracted from a laser cartography measurement procedure, by using a laser vibrometer (OFV 505 polytec). The response of the plate is measured successively in different known points of the surface and then are projected on the modal basis by
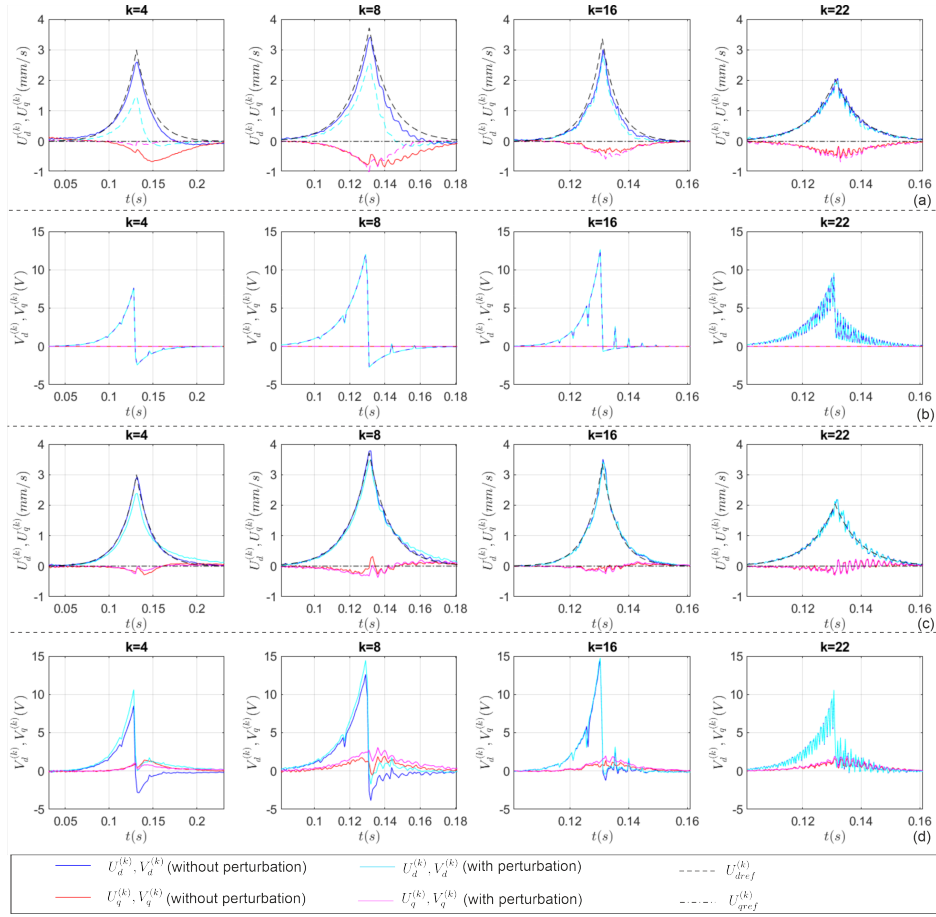
Figure 20: Modal signals in the demodulated bases for a focusing at the center of the plate, with $t_f = 131.1$ms :(a) Modal velocities components $U_d^{(k)}$ and $U_q^{(k)}$ in the case of just feedforward control $\mathbf{C_{ff}}$; (b) The associated voltages $V_d^{(k)}$ and $V_q^{(k)}$

using the identified mode shapes. The extracted modal velocities are shown in Fig.21. The Matlab command filtfilt is used in order to isolate the frequency components around the resonance of each mode and the corresponding signals are shown in red dashed lines. As shown in the figure, the references at the focusing time are reached, while all the modal velocities are in phase at their maximum for $t = t_f$. However, the components $\dot{\eta}^{(22)}$ show an error of around 20% which may be caused by the voltage ripple.

The modal responses in presence of external perturbation are shown in Fig.22. When the feedback control is applied (Fig.22.a), the modal velocities
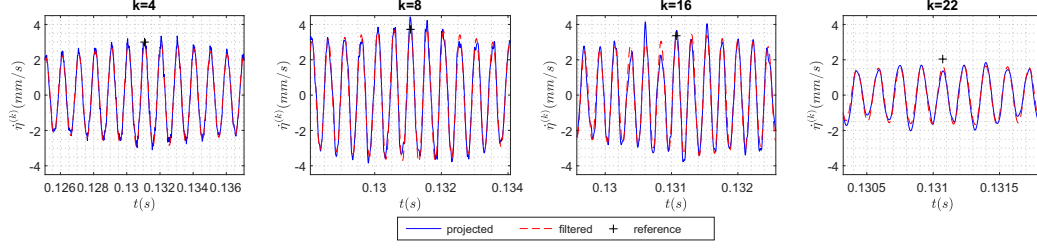
28

Figure 21: Extracted modal velocities $\dot{\eta}^{(k)}$ of the controlled modes in absence of external perturbation, the modal velocities reference at the focusing time $\dot{\eta}_f^{*(k)}$ are represented by the symbol +.

at the focusing time are slightly attenuated. However, when the feedback control is not applied, the modal velocities are much attenuated, with particularly $\dot{\eta}^{(4)}$.
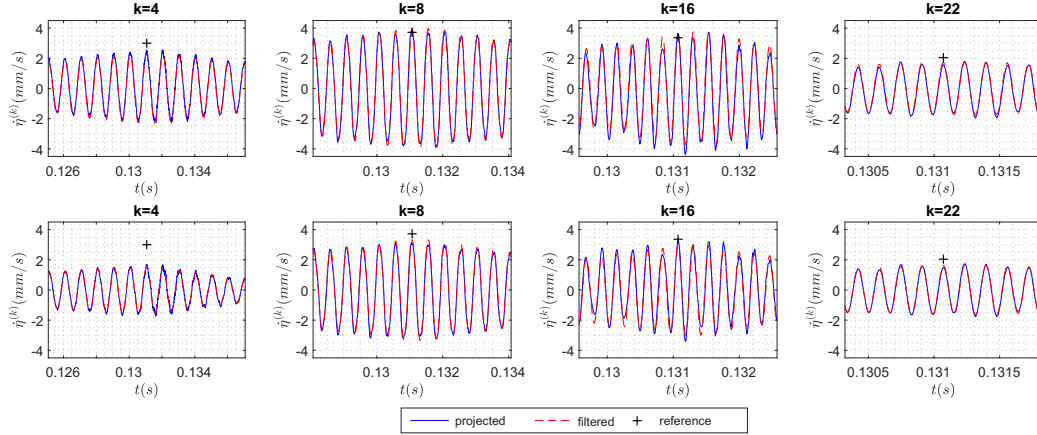

Figure 22: Extracted modal velocities $\dot{\eta}^{(k)}$ of the controlled modes in presence of external perturbation : (a) with feedback control (b) without feedback control

The influence of the external disturbance on the velocity field at the focusing time is shown in Fig.23. It can be observed that the velocity field is more attenuated in absence of feedback control than in its presence. The respective quadratic spatial errors are $\upsilon = 0.27$ (without feedback) and $\upsilon = 0.14$ (with feedback), where the quadratic spatial error between a specified velocity field $\dot{w}_s$ and the obtained one $\dot{w}_o$ is defined as follow :

29

$$v(\dot{w}_s, \dot{w}_o) = \left(\frac{\iint_{S_p} (\dot{w}_s(x,y) - \dot{w}_o(x,y))^2 \, dxdy}{\iint_{S_p} \dot{w}_s(x,y)^2 dxdy} \right)^{1/2} \tag{31}$$
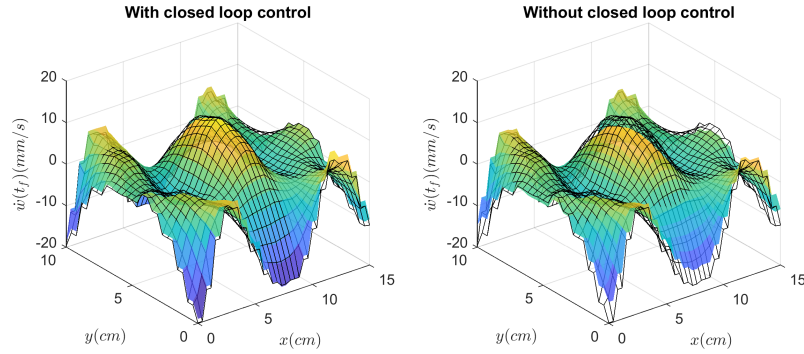

Figure 23: Velocity fields measured in the presence of external perturbation : (left) While using closed loop control bloc $\boldsymbol{C}_{fb}^{(k)}$, (right) without using closed loop control bloc $\boldsymbol{C}_{fb}^{(k)}$.

At this point, we demonstrate the validity of the proposed control structure in order to generate a focused velocity field, by using a modulated-demodulated control. The integration of feedback control allowed to reduce the tracking error when an external disturbance influences the system dynamic. Considering the used external set-up, only four modes can be controlled simultaneously. In order to reproduce the defined references shown in Fig.9, we control separately two sets of modes, $k \in \{4, 8, 16, 22\}$ and then $k \in \{6, 9, 12, 15\}$. For the second set, all the optimisation, filtering and controller design procedures are reapplied. For each set of modes, the velocity field is focused at the 'left', 'center' and at the 'right' of the plate. Then, since the system in linear, the results with each set of modes are superposed in order to reconstruct the velocity field as if all the modes could be controlled simultaneously.

The obtained velocity fields for each spatial references "right", "center" and "left" and using the first set of modes $k \in \{4, 8, 16, 22\}$ are shown in Fig. 24.(a). The obtained velocity fields with the second set of modes $k \in \{6, 9, 12, 15\}$ are shown in the Fig.24.(b). The superposition of both results as if we could control simultaneously all the selected 8 modes is shown
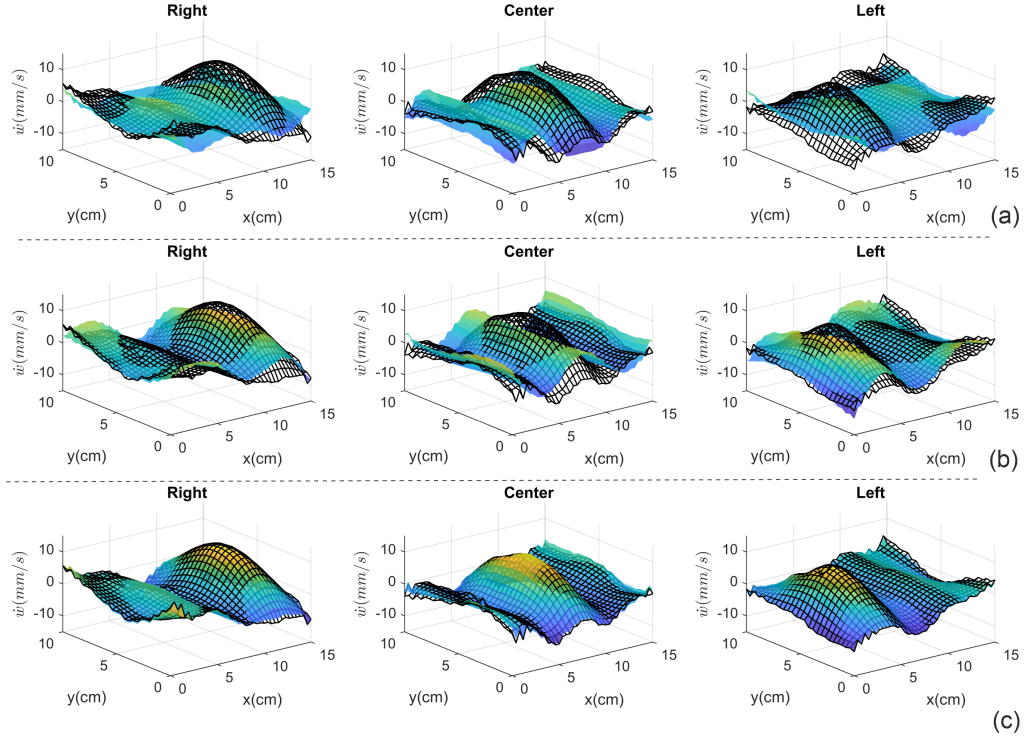
Figure 24: (a) Velocity fields with modes $\{4, 8, 16, 22\}$, (b) Velocity fields with modes $\{6, 9, 12, 15\}$, (c) reconstructed velocity fields with the two sets of modes "(c)=(a)+(b)"

in Fig.24.(c). As it can observed, the obtained velocity fields at the focusing time matches well with the references, where the corresponding spatial quadratic errors for "right", "center" and "left" reference are respectively $v_r = 0.10$, $v_c = 0.13$ and $v_l = 0.09$.

5. Discussion and conclusion

In this work, the modulated-demodulated control of one vibration mode is generalized to allow the simultaneous control of several vibration modes, thanks to the use of modal filters. A novel method to design the modal filter is proposed, it allows to take into account the influence of the frequency filter applied in downstream. In this context and compared with the classical calculation method for the modal filter coefficients, the proposed calculation method enhances the modal coordinates measurement quality which can be

a good solution in the case where the number of available sensors is limited. It is obvious that the efficiency of the proposed method depends directly on the distance between the resonance frequencies.

An experimental prototype of the control unit was developed for that purpose, it consists in a set of micro-controllers stm32f4, where each one is responsible to control a given number of modes. Since the micro-controllers possesses a limited number of inputs and outputs, hence the number of used actuators and sensors is limited. Then, different optimization procedures were performed in order to select the best sensors or actuators sets.

The proposed control approach has been applied to produce predefined velocity field within the framework of tactile feedback touchscreen, in order to generate localized tactile stimulation. The user finger in contact with the vibrating surface acts as a perturbation. The modulated-demodulated control showed a good rejection of the perturbation. It can be assumed that the rejection degree could be enhanced by enlarging the controller bandwidth with a higher choice of the acceleration factor.

Acknowledgement

References

[1] A. Preumont, Vibration Control of Active Structures: An Introduction, 4th Edition, Solid Mechanics and Its Applications, Springer International Publishing, 2018.

[2] J. P. Cleveland, B. Anczykowski, A. E. Schmid, V. B. Elings, Energy dissipation in tapping-mode atomic force microscopy, Applied Physics Letters 72 (20) (1998) 2613–2615.

[3] B. Borovic, A. Q. Liu, D. Popa, H. Cai, F. L. Lewis, Open-loop versus closed-loop control of MEMS devices: choices and issues, Journal of Micromechanics and Microengineering 15 (10) (2005) 1917–1924.

[4] W. B. Messaoud, F. Giraud, B. Lemaire-Semail, M. Amberg, M. Bueno, Amplitude control of an ultrasonic vibration for a tactile stimulator, IEEE/ASME Transactions on Mechatronics 21 (3) (2016) 1692–1701.

[5] S. Davis, I. Bucher, Automatic vibration mode selection and excitation; combining modal filtering with autoresonance, Mechanical Systems and Signal Processing 101 140–155.

[6] A. Bazaei, S. O. R. Moheimani, Synthesis of modulated–demodulated control systems, Automatica 50 (7) (2014) 1816–1824.

[7] D. Chen, B. E. Paden, Nonlinear adaptive torque-ripple cancellation for step motors, 29th IEEE Conference on Decision and Control (1990).

[8] M. Bodson, A. Sacks, P. Khosla, Harmonic generation in adaptive feed-forward cancellation schemes, IEEE Transactions on Automatic Control 39 (9) (1994) 1939–1944.

[9] F. Giraud, C. Giraud-Audine, Piezoelectric Actuators: Vector Control Method, Butterworth-Heinemann, 2019.

[10] S. Ghenna, F. Giraud, C. Giraud-Audine, M. Amberg, Vector control of piezoelectric transducers and ultrasonic actuators, IEEE Transactions on Industrial Electronics 65 (6) (2018) 4880–4888.

[11] R. Garcia, E. T. Herruzo, The emergence of multifrequency force microscopy, Nature Nanotechnology 7 (4) (2012) 217–226.

[12] K. Takemura, T. Maeno, Design and control of an ultrasonic motor capable of generating multi-DOF motion, IEEE/ASME Transactions on Mechatronics 6 (4) (2001) 499–506.

[13] E. Enferad, C. Giraud-Audine, F. Giraud, M. Amberg, B. Lemaire-Semail, Generating controlled localized stimulations on haptic displays by modal superimposition, Journal of Sound and Vibration 449 (2019) 196–213.

[14] R. M. Toyabur, M. Salauddin, J. Y. Park, Design and experiment of piezoelectric multimodal energy harvester for low frequency vibration, Ceramics International 43 (2017) S675–S681.

[15] R. M. Toyabur, M. Salauddin, H. Cho, J. Y. Park, A multimodal hybrid energy harvester based on piezoelectric-electromagnetic mechanisms for low-frequency ambient vibrations, Energy Conversion and Management 168 (2018) 454–466.

[16] A. Kaci, C. Giraud-Audine, F. Giraud, M. Amberg, B. Lemaire-Semail, LQR based MIMO-PID controller for the vector control of an underdamped harmonic oscillator, Mechanical Systems and Signal Processing 134 (2019) 106314.

[17] L. Meirovitch, Fundamentals of vibrations, McGraw-Hill, Boston, 2001.

[18] K. Lau, G. Goodwin, R. M'Closkey, Properties of modulated and demodulated systems with implications to feedback limitations, Automatica 41 (12) (2005) 2123–2129. `doi:10.1016/j.automatica.2005.07.009`.

[19] K. Lau, D. E. Quevedo, B. J. G. Vautier, G. C. Goodwin, S. O. R. Moheimani, Design of modulated and demodulated controllers for flexible structures, Control Engineering Practice 15 (3) (2007) 377–388.

[20] F. W. Fairman, Linear Control Theory: The State Space Approach, John Wiley & Sons, 1998.

[21] K. S. Karvinen, S. O. R. Moheimani, Modulated-demodulated q control of an atomic force microscope microcantilever, IFAC Proceedings Volumes 46 (5) (2013) 399–405.

[22] E. Enferad, C. Giraud-Audine, F. Giraud, M. Amberg, B. Lemaire-Semail, Differentiated haptic stimulation by modal synthesis of vibration field, IEEE Haptics Symposium (HAPTICS) (2018) 216–221.

[23] J. Monnoyer, E. Diaz, C. Bourdin, M. Wiertlewski, Perception of ultrasonic switches involves large discontinuity of the mechanical impedance, IEEE Transactions on Haptics 11 (4) (2018) 579–589.

[24] A. Kaci, A. Torres, F. Giraud, C. Giraud-Audine, M. Amberg, B. Lemaire-Semail, Fundamental acoustical finger force calculation for out-of-plane ultrasonic vibration and its correlation with friction reduction, 2019 IEEE World Haptics Conference (WHC) (2019) 413–418.

[25] M. Geradin, D. J. Rixen, Théorie des vibrations : application à la dynamique des structures, 1993.

[26] C. Rajalingham, R. B. Bhat, G. D. Xistris, VIBRATION OF RECTANGULAR PLATES USING PLATE CHARACTERISTIC FUNCTIONS

AS SHAPE FUNCTIONS IN THE RAYLEIGH–RITZ METHOD, Journal of Sound and Vibration 193.

[27] A. Hać, L. Liu, Sensor and actuator location in motion control of flexible structures, Journal of Sound and Vibration 167 (2) (1993) 239–261.

[28] S. Leleu, H. Abou-Kandil, Y. Bonnassieux, Piezoelectric actuators and sensors location for active control of flexible structures, IEEE Transactions on Instrumentation and Measurement 50 (6) (2001) 1577–1582.

[29] M. G. Ruppert, D. M. Harcombe, M. R. P. Ragazzon, S. O. R. Moheimani, A. J. Fleming, A review of demodulation techniques for amplitude-modulation atomic force microscopy, Beilstein Journal of Nanotechnology 8 (1) (2017) 1407–1426.

[30] A. Preumont, A. François, P. De Man, V. Piefort, Spatial filters in structural control, Journal of Sound and Vibration 265 (1) (2003) 61–79.

[31] J. He, Z.-F. Fu, Modal Analysis, Butterworth-Heinemann, 2001.